Fusion Engineering and Design 212 (2025) 114851

Contents lists available at ScienceDirect

Fusion Engineering and Design

journal homepage: www.elsevier.com/locate/fusengdes

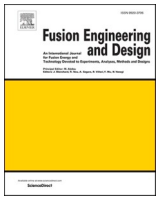

Rig design development for in situ tritium release studies of EU reference ceramic breeders (ACB-TREND)

A. Shaimerdenov [a], J. Leys [b,*], T. Kulsartov [a,c], D. Sairanbayev [a], Y. Chikhray [a,c], A. Akhanov [a], S. Askerbekov [a], M. Ionescu-Bujor [b], R. Knitter [b]

[a] The Institute of Nuclear Physics, Almaty, Kazakhstan
[b] Karlsruhe Institute of Technology, Karlsruhe, Germany
[c] al-Farabi Kazakh National University, Almaty, Kazakhstan

ARTICLE INFO

Keywords:
Advanced ceramic breeder
Neutron irradiation
Tritium release
Irradiation rig design

ABSTRACT

Advanced Ceramic Breeder (ACB) material is the European reference material for the ITER Test Blanket Module (TBM) and the DEMO Helium Cooled Pebble Bed (HCPB) blanket concept. The biphasic ACB material (Li_4SiO_4 + Li_2TiO_3) has been extensively characterised and evaluated in the past. However, the ACB's in situ performance under neutron irradiation still has to be investigated in detail. Therefore, the "Advanced Ceramic Breeder's in situ Tritium Release Experiment under Neutron irraDiation" (ACB-TREND) campaign was launched. For the irradiation taking place in the WWR-K research reactor, an irradiation rig (IR) design was developed that is presented here. The IR design needs to meet certain criteria that allows more fusion-like irradiation conditions. A cadmium shielding will be used to reduce the thermal neutrons to decrease the lithium burn-up significantly. The IR design was evaluated in a mock-up test. Small adaptions were made to completely cover the desired temperature range of 400–900 °C.

1. Introduction

Advanced Ceramic Breeder (ACB) material in the form of pebbles is the European reference material for the ITER Test Blanket Module (TBM) and the DEMO Helium Cooled Pebble Bed (HCPB) blanket concept. ACB is a biphasic material consisting of lithium orthosilicate (Li_4SiO_4, LOS) with additions of lithium metatitanate (Li_2TiO_3, LMT). ACB pebbles are produced using the melt-based KALOS process [1,2]. While the material properties were comprehensively studied in the past [2–7], only short, preliminary neutron irradiation experiments were performed so far [8–12]. As the tritium release performance of ACB pebbles under neutron irradiation is an essential issue, ACB pebbles the "Advanced Ceramic Breeder's in situ Tritium Release Experiment under Neutron irraDiation" (ACB-TREND) campaign was launched. The ACB pebbles will be irradiated at the WWR-K research reactor [13,14] and the tritium release behaviour will be studied in situ. In contrast to previous shorter experiments, the ACB samples are enriched in lithium-6 and the neutron spectrum of the research reactor will be adapted to more fusion-like conditions. This campaign is the European part of irradiation experiments planned within the Broader Approach DEMO by KIT, while another irradiation campaign at the WWR-K reactor is organised for Japan by QST (National Institutes for Quantum Science and Technology).

For ACB-TREND, parameters were chosen to simulate ITER-like conditions. This means a relatively low lithium burn-up and low damage level with a ratio of about 0.7. The tritium release will be investigated in the temperature range from 400 to 900 °C. Moreover, different purge gas compositions shall be tested using pure helium and helium with different additions of hydrogen. In the experiment, the tritium release will be measured in situ distinguishing the tritium species HT and HTO. Subsequently, the tritium residence time will be determined.

This work presents the technical preparation and in particular the development of the irradiation rig (IR) design for the ACB-TREND campaign to fulfil the requirements of the irradiation parameters and fusion-like conditions in a fission reactor.

* Corresponding author.
E-mail address: julia.leys@kit.edu (J. Leys).

https://doi.org/10.1016/j.fusengdes.2025.114851
Received 21 November 2024; Received in revised form 31 January 2025; Accepted 31 January 2025
Available online 6 February 2025

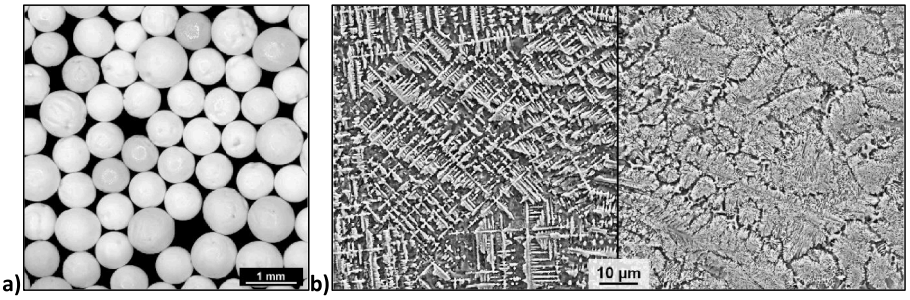

Fig. 1. a) Light microscope image and b) SEM images of characteristic microstructures of the ACB pebbles 30-LMT-90.

Table 1
Material properties of ACB pebble sample 30-LMT-90. (referring to a theoretical density of 2.605 g/cm^3 considering the actual chemical composition and densities of Li_4SiO_4 [15] and Li_2TiO_3 [16].).

Property	LMT / mol %	Li-6 / at%	Closed porosity / %	Open porosity / %	Pour density / g•cm^{-3}	Tap density / g•cm^{-3}	Crush load / N (Ø=710 and 1000 µm)	Pebble size / µm
Actual value	28.3 ± 0.4	88.97 ±0.04	4.0 ± 0.1	2.2 ± 0.2	1.35±0.03	1.53±0.03	10.5 ± 4.0 19.0 ± 8.0	500–1000

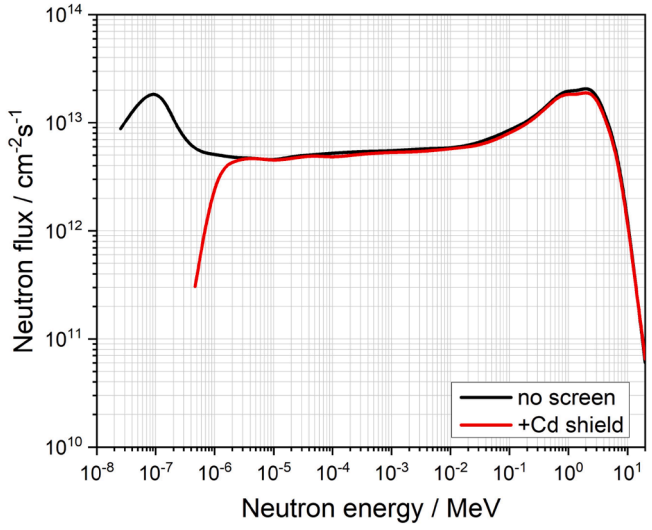

Fig. 2. Typical neutron spectrum in a core position without (black) and with Cd shielding (red).

2. Materials and methods

2.1. Samples and reactor conditions

Biphasic ACB material consisting of nominal 70 mol% LOS and 30 mol% LMT with a Li-6 enrichment of nominal 90 at% (hereinafter referred to as '30-LMT-90') were selected for the ACB-TREND campaign (see Fig. 1). Pebbles were produced with the KALOS process using high purity raw materials of lithium hydroxide monohydrate ($LiOH•H_2O$), silicon dioxide (SiO_2), and titanium dioxide (TiO_2). To obtain the desired lithium-6 enrichment, $LiOH•H_2O$ (with 95 at% Li-6) purchased from Sigma Aldrich was considered in the respective portion. The pebbles that have a wide size range after production were screened to a size range of 500 to 1000 µm. More detailed material properties of the 30-LMT-90 pebbles are summarised in Table 1.

For the experiment the material shall be irradiated in two independent capsules including 2 g of ACB pebble beds (PB) in each capsule. The tritium release behaviour shall be investigated in two different temperature ranges, one range per capsule (low temperature (LT): 400–600 °C and high temperature (HT): 600–900 °C). For both temperature ranges, the influence of the purge gas composition shall be studied. Therefore, pure helium and helium with different additions of hydrogen will be controllably purged into the capsules (He + x % H_2 with x = 0–0.2 vol%). For each capsule, three cycles of 20–21 days are planned in which the temperature and purge gas composition will be varied.

Table 2
Reactor conditions in the WWR-K reactor (core position; no shielding for thermal neutrons) in comparison to the ITER TBM considering 30-LMT-90 [17].

Parameter	WWR-K (core)	ITER TBM
dpa/FPY	350	7.1
Li burn-up/FPY / %	48.5	4.9
Li burn-up/dpa ratio	0.14	0.7
Contribution E < 0.1 eV / %	89	16
Flux <0.1 eV / %	41	0.3
Total flux / × 10^{14} n•cm^{-2}•s^{-1}	3.2	1.9

To simulate more fusion-like and in particular more ITER-like conditions, the neutron spectrum of the fission research reactor needs to be adapted. This means in particular that the high number of thermal neutrons that occur in a fission reactor needs to be reduced. To cut off thermal neutrons, different shielding materials were considered. Cadmium was chosen as most favourable shielding material due its specific nuclear-physical properties. Fig. 2 shows the comparison of the unshielded and Cd-shielded neutron spectrum in the WWR-K research reactor.

Several parameters in ITER and the WWR-K were calculated and compared [17] in order to know how the irradiation device needs to be built to approximate as much as possible the desired values. Table 2 summarises the reactor conditions of the WWR-K reactor (core position, no shielding) and the ITER TBM with regard to the 30-LMT-90 material.

2.2. Method for neutron-physical calculations

Neutron-physical calculations were carried out using the Monte-Carlo code MCNP® (version MCNP6) [18] equipped with the ENDF/B-VII library for nuclear cross sections [19]. The purpose of the calculations was to determine the following parameters (statistical error is given in brackets):

Table 3
Relevant nuclear reactions considered in dpa calculations for the two phases in the ACB material.

	Li-6	Li-7	Si	Ti	O-16
Li_4SiO_4	elast. (n,n'), (n,t)	elast. (n,n')	elast. (n,n'), (n,p)	—	elast. (n,n')
Li_2TiO_3	elast. (n,n'), (n,t)	elast. (n,n')	—	elast. (n,n'), (n,2n)	elast. (n,n')

- Radiation heating in samples and the structural materials of the IR (≤ 4 %)
- Neutron flux density on the samples (8 % on average)
- Burn-up of lithium in the samples (~1.5 %)
- Number of defects (displacements per atom (dpa)) in the samples (~1 %)
- Tritium activity (~1.5 %)

In the MCNP6 simulations the actual state of the WWR-K reactor core was considered (i.e. core configuration, burn-up in the fuel assembly and poisoning of the beryllium reflector). Furthermore, the IR is located in a periphery cell of the reactor core at the boundary between the nuclear fuel and the beryllium reflector. Any radial non-uniformity can be neglected due to the small sample diameter. In the calculation of the energy release, also the delayed gamma radiation emitted by the uranium fission fragments was considered.

For the calculations of the lithium burn-up in the ACB sample the following main reactions were considered:

$$^{6}\mathrm{Li} + \mathrm{n} \rightarrow \mathrm{T} + {}^{4}\mathrm{He} + 4.78\,\mathrm{MeV} \quad (1)$$

$$^{7}\mathrm{Li} + \mathrm{n} \rightarrow \mathrm{T} + {}^{4}\mathrm{He} + \mathrm{n}' - 2.47\,\mathrm{MeV} \quad (2)$$

For the reaction regarding Eq. (1) the microscopic cross section is approximately 940 barns for thermal neutrons, while the cross section for the nuclear reaction regarding Eq. (2) does not exceed 0.4 barns (threshold reaction) [20]. The WWR-K reactor has a predominantly thermal energy spectrum of neutrons, which would lead to an intense nuclear reaction with regard to Eq. (1) in the ACB sample. Considering that the ACB sample 30-LMT-90 exhibits a very high enrichment in lithium-6 of 90 at%, the lithium burn-up is determined by the burn-up of lithium-6 and hence by the nuclear reaction given in Eq. (1).

To calculate the damage level in the sample, the cross sections of ceramic breeder materials by Leichtle were considered [21]. In a first step the neutron flux density was calculated for 100 energy groups of the energy spectrum. In a second step, the dpa formation rate in lithium ceramics and the dpa for one operational cycle in the WWR-K reactor was determined using Eq. (3).

$$\frac{R}{N} = \frac{\mathrm{dpa}}{\mathrm{s}} = \int_{0}^{E_{\max}} \phi(E_i)\cdot\sigma_{\mathrm{D}}(E_i)\boldsymbol{d}E_i \quad (3)$$

where R is the dpa rate (displacement·m^{-3}·s^{-1}), N is the atomic density (atoms·m^{-3}), σ_D is the displacement cross section, and $\phi(E_i)$ is the flux distribution depending on the energy.

Damage cross sections for the two phases Li_4SiO_4 and Li_2TiO_3 in the ACB material were provided by Leichtle [22]. For the calculations of the dpa the reactions given in Table 3 were considered.

2.3. Method for thermophysical calculations

Thermophysical calculations were performed using the simulation software COMSOL Multiphysics® [23]. An analytical system of fundamental heat transfer equations was used considering the thermal conductivity, convection and thermal radiation. In the present case, a non-isothermal flow module was used that combines the equations of thermal conductivity in solid and liquid (gaseous) media with the Navier-Stokes equation for laminar or turbulent flow of cooling gases or water flows.

The following Eqs. (4–5) of heat conduction and convection were used:

$$\rho C_{\mathrm{p}}\frac{\partial T}{\partial t} + \rho C_{\mathrm{p}}\boldsymbol{u}\cdot\nabla T + \nabla\cdot\boldsymbol{q} = Q + Q_{\mathrm{p}} + Q_{\mathrm{vd}} \quad (4)$$

$$\boldsymbol{q} = -k\nabla T \quad (5)$$

where: ρ – density (kg•cm^{-3}); C_p – specific heat capacity at constant pressure (J•kg^{-1}•K^{-1}); T – absolute temperature (K); $\boldsymbol{u}$ – velocity vector (m•s^{-1}); $\boldsymbol{q}$ – heat flow vector in (W•m^{-2}); Q – internal heat source (W•m^{-3}); Q_p – heat caused by pressure (W•m^{-3}); Q_{vd} – heat of internal friction (W•m^{-3}); k – thermal conductivity (W•m^{-1}•K^{-1}).

For heat transfer by radiation (surfaces) the Eqs. (6–11) and for the laminar flow the Eqs. (12–13) that are the Navier-Stokes equations for the conservation of momentum and the conservation of mass were used:

$$-\boldsymbol{n}\cdot\boldsymbol{q} = \varepsilon(G - e_{\mathrm{b}}(T)) \quad (6)$$

$$(1-\varepsilon)G = J - \varepsilon e_{\mathrm{b}}(T) \quad (7)$$

$$G = G_{\mathrm{m}}(J) + G_{\mathrm{amb}} + G_{\mathrm{ext}} \quad (8)$$

$$G_{\mathrm{amb}} = F_{\mathrm{amb}}e_{\mathrm{b}}(T_{\mathrm{amb}}) \quad (9)$$

$$G_{\mathrm{ext}} = G_{\mathrm{extDir}} + G_{\mathrm{extDiff}} \quad (10)$$

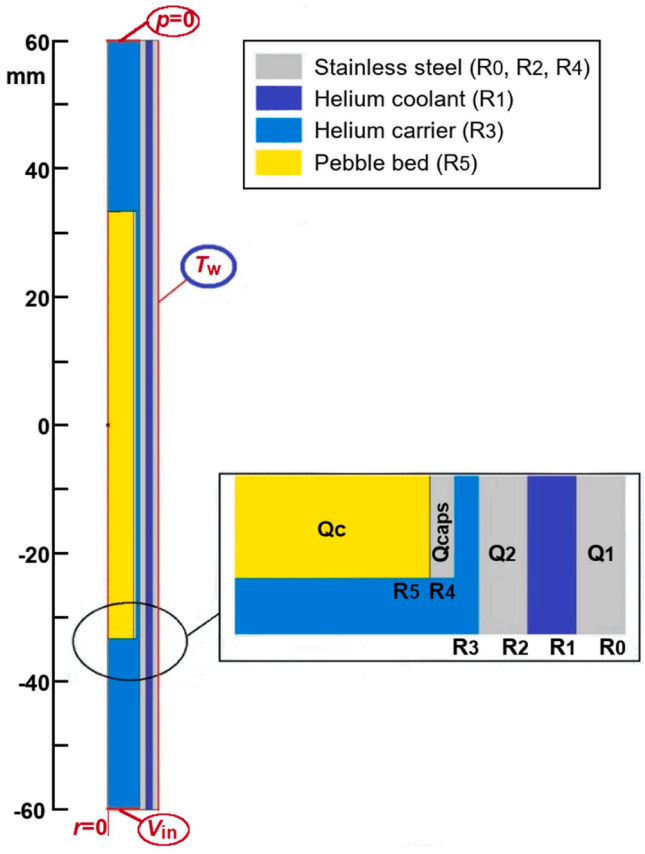

Fig. 3. Main domains of the model indicating boundary conditions, heat sources and radius designations.

$$e_b(T) = n^2\sigma T^4 \tag{11}$$

$$\rho\frac{\partial \boldsymbol{u}}{\partial t} + \rho(\boldsymbol{u}\cdot\nabla)\boldsymbol{u} = \nabla\cdot\left[-\rho\boldsymbol{I} + \mu\left(\nabla\boldsymbol{u} + (\nabla\boldsymbol{u})^T\right) - \frac{2}{3}\mu(\nabla\cdot\boldsymbol{u})\boldsymbol{I}\right] + \boldsymbol{F} + \rho\boldsymbol{g} \tag{12}$$

$$\frac{\partial \rho}{\partial t} + \nabla\cdot(\rho\boldsymbol{u}) = 0 \tag{13}$$

where: $\boldsymbol{n}$ – normal vector outward; ε – surface emissivity (dimensionless); μ – dynamic viscosity (Pa•s), G – incident flux (W•m^{-2}); $e_b(T)$ – total black body radiation power (W•m^{-2}); J – radiation flux (W•m^{-2}); G_m – mutual surface radiation (W•m^{-2}); G_{amb} – environment flux (W•m^{-2}); G_{ext} – external flow (W•m^{-2}); F_{amb} – appearance factor (dimensionless); T_{amb} – ambient temperature (K); G_{extDir} – direct component of external radiation (W•m^{-2}); $G_{extDiff}$ – diffuse (scattered) component of external radiation (W•m^{-2}); n – refractive index for a transparent medium (dimensionless), σ – Stefan-Boltzmann constant (W•m^{-2}•K^{-4}); ∇ – differentiation operator, Nabla (m^{-1}); $\boldsymbol{I}$ – unit tensor (dimensionless); $\boldsymbol{F}$ – volume force vector (N•m^{-3}); $\boldsymbol{g}$ – gravity acceleration (m^2•s^{-1}).

The ACB PB was simulated as a porous media with 63 vol% of ceramics and with an average thermal conductivity coefficient (37 vol% pores filled with helium). Emissive surfaces are described as radiating diffusively only outward, but receiving similar radiation from other surfaces. The temperatures of the sample and the structural materials of the IR, as well as the temperature gradient throughout the PB's volume, were estimated by calculation.

Thermal calculations were carried out for two different helium gas pressures in the thermal gap of the IR: 10 and 10^5 Pa referring to the maximum and the minimum temperature, respectively.

First thermophysical calculations were refined for the favoured IR design option. A limited axisymmetric representation of the IR and its geometry was developed. Fig. 3 shows the geometry of the IR indicating the main domains and their materials and the heat sources in them. It was assumed that the IR is cooled by water from the reactor cooling system and the surface temperature of the outer wall R0 is fixed and has a temperature of 40 °C (i.e. T_w in Fig. 3).

The standard library of COMSOL was used for the different materials: Li_4SiO_4, Li_2TiO_3, helium and stainless steel (SS 316LN was selected as an analogue of 12Cr18Ni10Ti stainless steel). Parameters such as thermal conductivity, dynamic viscosity, specific heat capacity at constant pressure and density were implemented from the library.

A calculation of the stationary distribution of temperatures and gas flow was carried out (using stationary mode in COMSOL). It is assumed that there is no convection in the helium cooling circuit and its absolute pressure can vary from 10 to 1.5×10^5 Pa, which is used to control the heat transfer coefficient and the cooling flow (temperature) of the sample capsule.

The PG is purged from the bottom to the top with a flow rate of 0.1 l·min^{-1} (i.e. V_{in} in Fig. 3). The PG supply is located at the bottom side of R3 domain and exits at the opposite boundary at the top meeting 'pressure-free' conditions (i.e. $p = 0$ in Fig. 3). Helium as the PG is described as an incompressible, non-isothermal gas moving laminarly in the lower and upper parts of the domain and in the gap between the capsule wall (R4) and the tube (R3) (see Fig. 3). Darcy's law is considered as a part of the PG flow passes through the PB (see Eq. (14)).

$$V_{in} = \frac{k_p A}{\mu h}\Delta p \tag{14}$$

where: V_{in} – He flow rate (m^3•s^{-1}); Δp – He pressure drop across the height h of the PB; A – cross-sectional area of the He gas supply into the PB; k_p – PB permeability (m^2), which is assumed to be 6.3×10^{-10} m^2 according to [24]; μ – dynamic viscosity of He.

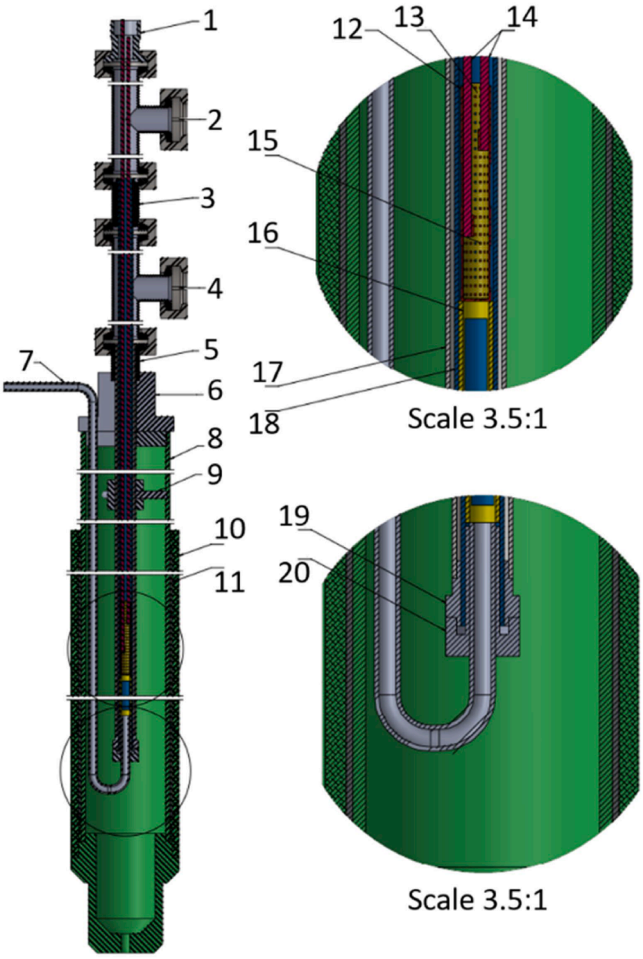

Fig. 4. Favoured IR design option with the following components: 1) Sealed lead-in 2) pumping path 3) fitting KF16 4) coolant (helium) path 5) direct fitting KF16 6) holder 7) purge gas path 8) channel 9) spacer 10) displacer 11) cadmium 12) capsule 13) platinum mesh 14) thermocouples 15) sample location 16) support 17) external channel 18) internal capsule 19) upper shim 20) bottom shim.

3. Results and discussion

3.1. Design of the irradiation rig

In a first step five options were considered with regard to pure Li_2TiO_3 as this was the material to be tested in the mock-up tests (provided by QST). In four cases, the capsule has a cylindrical shape with different dimensions, while in one case the capsule has the shape of a hollow cylinder. The volumes were chosen to fit about 2 g of ceramic pebbles in each capsule. Considering the results from neutron-physical calculations, one of the five options was favoured.

The suggested design option for the IR is shown in Fig. 4. The IR is a double-circuit sealed system: both, inner and outer circuits are filled with helium, but the inner circuit will be purged with the desired PG compositions during the irradiation experiment. A capsule including the sample is installed inside the IR. While the capsule in total is U-shaped, the sample geometry is cylindrical ($h = 47$ mm, $Ø = 6$ mm). The IR body with flanges, capsule and gas tubes is made of stainless steel. The inner surface of the capsule is covered with a platinum foil/mesh to prevent a reaction of the ACB sample with the structural material of the capsule. The capsule has two gas paths: one serving as the PG supply during the experiment and another one to pump the PG to the measurement equipment. The PG supply to the capsule is located at the bottom. The outer casing of the IR has one gas tube, which is designed to regulate the

Table 4
Calculated energy release in the IR elements for the selected IR design option.

Sample 30-LMT-90	Inner capsule	Outer capsule	Al alloy channel	Cd shielding
32.3 W•g^{-1}	1.3 W•g^{-1}	1.3 W•g^{-1}	1.2 W•g^{-1}	15.0 W•g^{-1}

Table 5
Neutron flux density in the sample volume for the favoured IR design option; $\Delta\varphi$ represents the relevant error.

Group number	Energy range / MeV			Sample 30-LMT-90	
				φ / cm^{-2}·s^{-1}	$\Delta\varphi$
1	0	–	2.52E-08	2.42E+11	0.04
2	2.52E-08	–	2.15E-07	2.15E+12	0.02
3	2.15E-07	–	4.65E-07	5.96E+11	0.06
4	4.65E-07	–	1.00E-06	7.78E+11	0.06
5	1.00E-06	–	2.15E-06	1.04E+12	0.06
6	2.15E-06	–	4.65E-06	1.14E+12	0.06
7	4.65E-06	–	1.00E-05	1.47E+12	0.05
8	1.00E-05	–	2.15E-05	1.66E+12	0.06
9	2.15E-05	–	4.65E-05	1.99E+12	0.06
10	4.65E-05	–	1.00E-04	1.90E+12	0.05
11	1.00E-04	–	2.15E-04	1.91E+12	0.06
12	2.15E-04	–	4.65E-04	2.06E+12	0.06
13	4.65E-04	–	1.00E-03	2.17E+12	0.05
14	1.00E-03	–	2.15E-03	2.28E+12	0.05
15	2.15E-03	–	4.65E-03	2.31E+12	0.06
16	4.65E-03	–	1.00E-02	2.22E+12	0.05
17	1.00E-02	–	2.00E-02	2.24E+12	0.06
18	2.00E-02	–	5.00E-02	2.33E+12	0.06
19	5.00E-02	–	1.00E-01	2.46E+12	0.05
20	1.00E-01	–	2.00E-01	3.51E+12	0.05
21	2.00E-01	–	4.00E-01	4.62E+12	0.04
22	4.00E-01	–	8.00E-01	5.69E+12	0.03
23	8.00E-01	–	1.40E+00	5.48E+12	0.04
24	1.40E+00	–	2.50E+00	6.18E+12	0.03
25	2.50E+00	–	4.00E+00	3.32E+12	0.04
26	4.00E+00	–	6.50E+00	1.68E+12	0.06
27	6.50E+00	–	1.05E+01	4.26E+11	0.13
28	1.05E+01	–	2.00E+01	9.58E+09	0.28
Integral				**6.39E+13**	

pressure and to control the temperature. At the outside of the IR, between the standard displacer and the aluminium channel, a cadmium screen with a thickness of 1 mm is installed to cut off the thermal neutrons from the sample. Inside the channel circulates the reactor primary circuit water. Two K-type thermocouples will be implemented in the capsule. One is located behind the platinum foil at a height of 15 mm from the top (not in direct contact with the ACB), while the other is positioned in a central position in the PB at a height of 15 mm from the bottom.

The option of implementing passive neutron flux sensors (fluence monitors) within the IR is given. They were implemented for the mock-up test to examine their practicability (see subSection 3.4).

The following advantages of the IR design option were considered:

- Compliance with the requirements of the technical specification
- Reliability and ease of maintenance
- Possibility of repeated use by replacing only the internal sample capsule

3.2. Neutron-physical calculations

Neutron-physical calculations for the 30-LMT-90 sample in the favoured IR design option were performed to determine the radiation heating in the ACB sample and the IR structural materials, the neutron flux densities (φ), the lithium burn-up, the damage level (dpa), and the tritium activity. The results on the energy release in the ACB sample and the different materials of the IR are given in Table 4 for the selected design option.

Table 6
Results on the lithium burn-up and the dpa in the ACB sample and the tritium activity corresponding to one irradiation cycle in the reactor.

Lithium-6 burn-up / %	dpa	Li-6 burn-up/dpa ratio	Tritium activity / Bq
0.43	0.34	1.27	2.58E+11

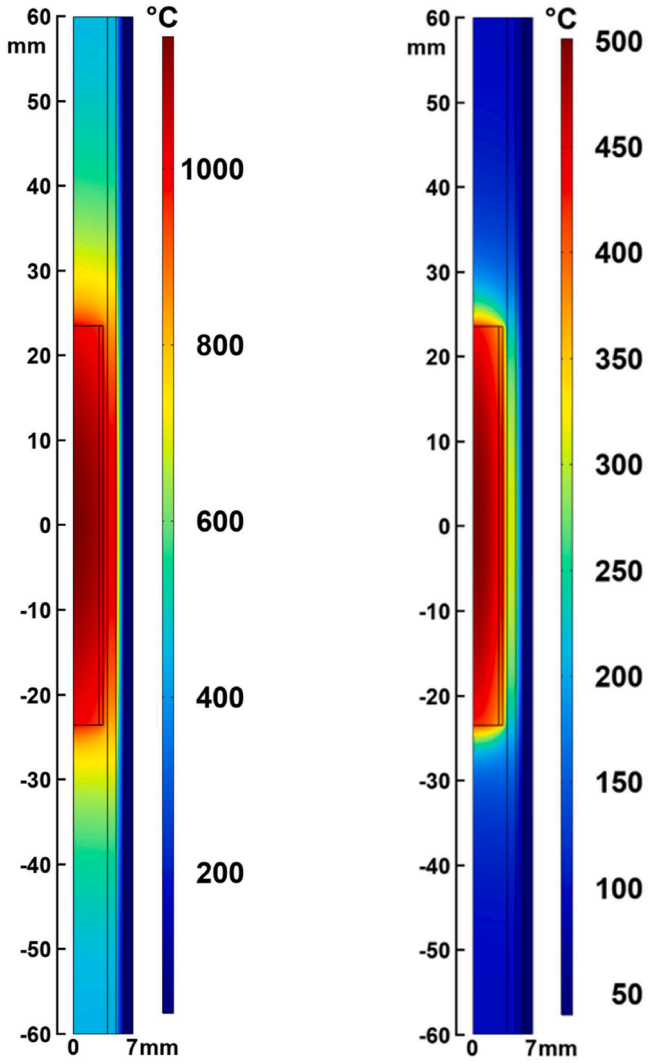

Fig. 5. Steady-state temperature distribution in the IR at 10 Pa (left) and 10^5 Pa (right) helium cooling for option-A.

The neutron flux densities in the volume of the ACB PB were determined for 28 energy groups of the neutron spectrum. The calculation results on the neutron flux density for the ACB sample 30-LMT-90 with regard to the favoured design option is shown in Table 5.

The results on the lithium burn-up and the damage level in the ACB material, as well as the tritium activity are summarised in Table 6. In addition, the ratio of lithium burn-up to dpa is given. The given tritium activity was determined only by the nuclear reaction in Eq. (1).

The given dpa value of 0.34 corresponds to the average volumetric value over the entire PB. However, it should be noted that the dpa on the surface of the PB equals 2.98. The dpa value is not affected significantly by the thickness of the cadmium shield that will be implemented in the IR. For example, for the favoured IR design option including a cadmium shield with a thickness of 0.5 mm the dpa value is 0.36, for a thickness of 1.0 mm the dpa equals 0.34, and for a thickness of 1.5 mm the dpa

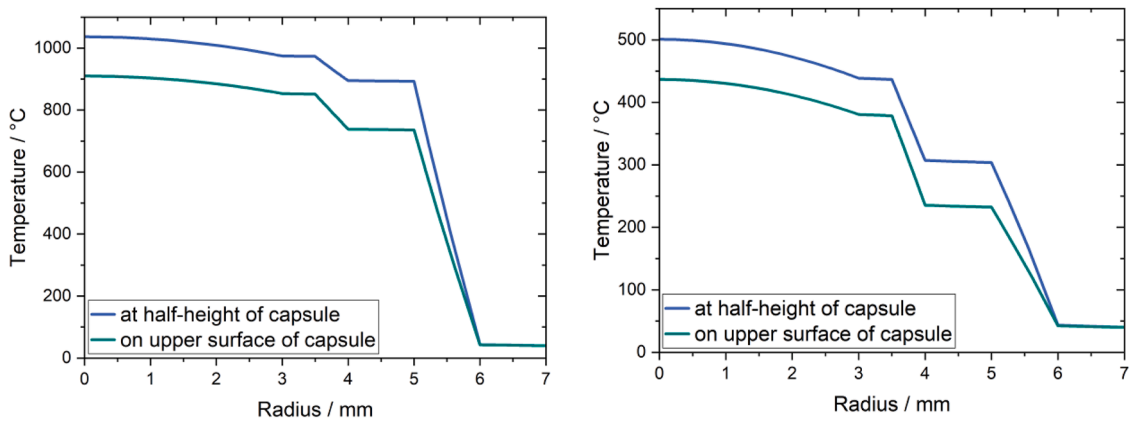

Fig. 6. Radial temperature distribution in the IR at 10 Pa (left) and 10^5 Pa (right) helium cooling for option-A. Blue: at half-height of the capsule; green: on the upper surface of the capsule.

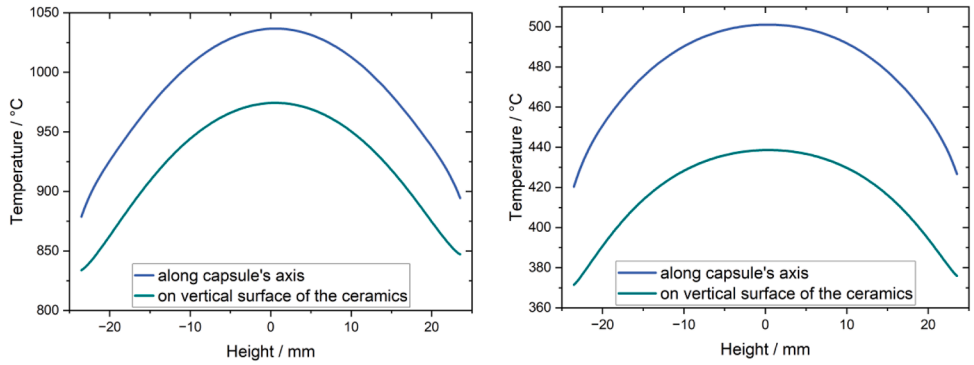

Fig. 7. Vertical temperature distribution in the IR at 10 Pa (left) and 10^5 Pa (right) helium cooling for option-A. Blue: along the capsule's axis; green: on the vertical surface of the ACB.

equals 0.33. An effect resulting from the burn-up of the cadmium can also be neglected due to the intended, relatively short irradiation times.

3.3. Thermophysical calculations

Temperature distributions for the ACB sample 30-LMT-90 in the favoured IR design option were calculated and are shown in Figs. 5–7.

Varying the helium gas pressure, it was estimated by calculations to achieve the lowest and highest desired temperatures. In the case using a helium gas pressure of 10 Pa, the average temperature of the ACB pebbles calculated by volume integration is 1067 °C. The average deviation of temperature over the entire ACB volume is ±41 °C. The speed of helium gas in the PB is 1.8 cm·s^{-1}. When using a helium gas pressure of 10^5 Pa, the average temperature of the ACB pebbles is 447 °C with an average deviation of ±22 °C over the ACB volume and a helium gas speed of 0.75 cm·s^{-1} in the PB.

These results for the favoured IR option almost cover the required temperature range completely. The highest desired temperature of 900 °C seems to be achievable by using a helium gas pressure of 10 Pa. However, the calculations show that the lowest desired temperature of 400 °C cannot be reached with a helium gas pressure of 10^5 Pa.

The decisive factor ensuring the normal temperature regime of the ACB samples is the thermal conductivity of the PB, which can affect the temperature regime of the samples. The influence of the "cold" PG on the temperature regime of the samples is not completely clear. A prediction of such a parameter was difficult to calculate and was tested during the mock-up test.

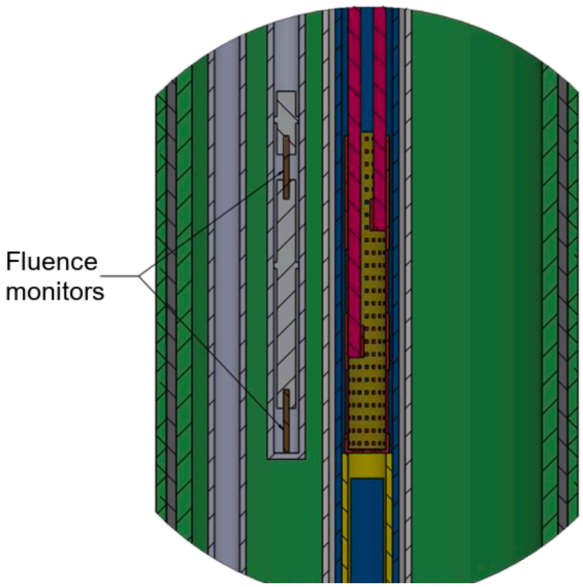

Fig. 8. Locations of the fluence monitors (compare Fig. 4).

3.4. Mock-up test and adjustments to the IR design

The performance of the favoured IR design option was analysed in a mock-up test during 16 days of irradiation in a representative irradiation cell of the reactor. Li_2TiO_3 pebbles enriched in lithium-6 by 95 at%

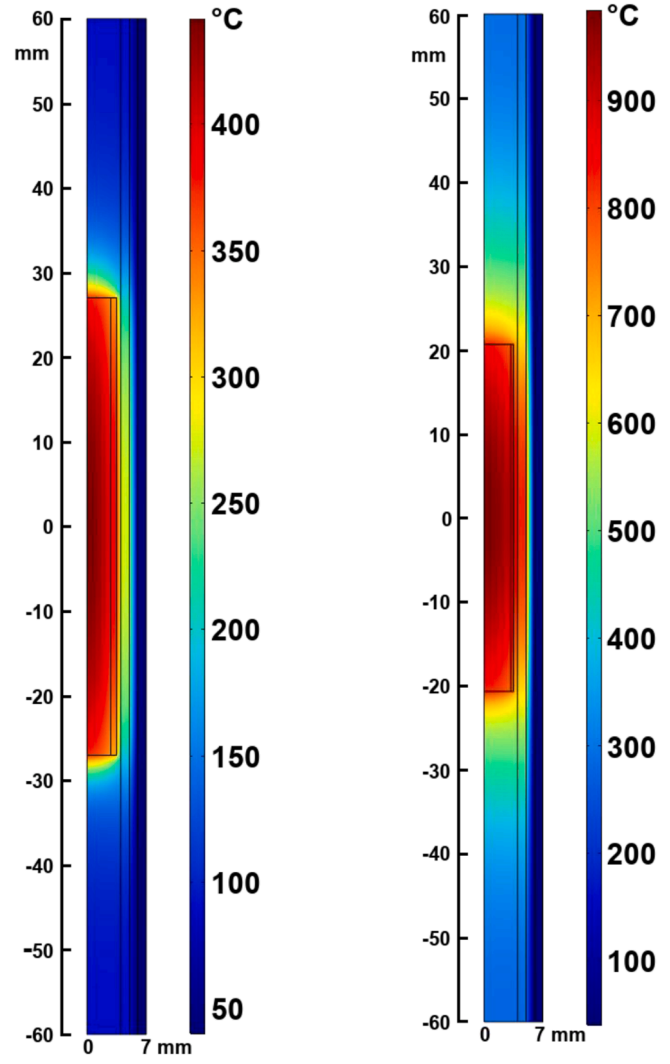

Fig. 9. Temperature distributions in the capsule with a wall thickness of 0.7 mm to reach the min. temperature in the LT-range (left) and with a wall thickness of 0.3 mm to reach the max. temperature in the HT-range (right).

provided by QST were used as ceramic breeder material for the mock-up test. The test was performed to verify the neutronic and thermophysical calculations, to measure the fluence of thermal and fast neutrons in the capsule and to test the functionality of the tritium utilisation system. The main objective with regard to the ceramic breeder was to test if the minimum target and maximum target temperatures of 400±20 °C and 900±45 °C, respectively, can be achieved.

During the mock-up test, fluence monitors were added to the IR design to measure the neutron flux density. Iron-based monitors were used to measure the fluence of fast neutrons (≥1.0 MeV), while monitors made of aluminium cobalt alloy (Al-0.475%Co) were used to measure the fluence of the thermal neutrons (≤0.683 eV). Two fluence monitors of each kind were implemented inside the irradiation channel between the purge gas supply and the outer channel including the capsule with the sample. Their positions were stretched along the height of the PB sample (see Fig. 8). In general, the experimental and the calculated fluence values are in good agreement. In three cases, the experimental fluence determination is by a factor of 1.3 higher than the fluence calculations. Only the upper fluence monitor for thermal neutrons revealed values in the experiment that are higher by a factor of 1.8, which is due to the spatial deviation (radial) of the monitor in the guide tube during irradiation.

The mock-up test revealed that the average temperature at about 10^5 Pa helium gas pressure was 425±30 °C and at <10 Pa was 878±37 °C. Therefore, the minimum and maximum of the desired temperature range could almost be covered, but still the minimum and maximum could not be reached. This is why the following adjustments are suggested.

For the irradiation in the LT-range the wall thickness of the capsule enclosing the ACB sample will be increased by 0.2 mm to be able to achieve the minimum target temperature of 400 °C. With this the internal diameter of the capsule is reduced from 6.0 to 5.6 mm while the height is changed from 47 to 54 mm keeping the diameter of the outer capsule constant at 7 mm. All other dimensions of IR will remain the same. Thermophysical calculations showed that the average temperature in the capsule with a wall thickness of 0.7 mm (instead of 0.5 mm) will be 397±19 °C. The temperature distribution inside the adjusted IR for the LT-range is shown in Fig. 9, left.

For the irradiation in the HT-range the wall thickness of the capsule will be decreased by 0.2 mm to enable the maximum target temperature of 900 °C. As a result, the internal diameter of the capsule is increased from 6.0 to 6.4 mm while the height is changed from 47 to 41 mm keeping the diameter of the outer capsule constant at 7 mm. All other dimensions of IR will remain the same. The average temperature in the capsule with a wall thickness of 0.3 mm (instead of 0.5 mm) was simulated to be 899±41 °C. The temperature distribution inside the adjusted IR for the LT-range is shown in Fig. 9, right.

4. Conclusions

One out of five irradiation rig design options was selected for the neutron irradiation of ACB pebbles within the ACB-TREND campaign. ACB pebbles consisting of nominal 70 mol% Li_4SiO_4 and 30 mol% Li_2TiO_3 with 90 at% lithium-6 will be used for the irradiation experiment. The irradiation rig design offers a volume to irradiate a pebble bed of ~2 g per capsule. Two capsules will be irradiated independently within a low (LT, 400–600 °C) and a high temperature (HT, 600–900 °C) range, while the samples are purged with different gas compositions (He + x % H_2). For each capsule, three irradiation cycles are foreseen in which the temperature and purge gas composition will be varied. Comprehensive neutron-physical and thermophysical calculations were performed. The lithium burn-up will be 0.43 %, the damage level 0.34 dpa, and the tritium activity 2.58 × 10^{11} Bq per irradiation cycle. The energy release calculated in the sample will be 32.3 W•g^{-1}. First calculations showed that the lowest target temperature of 400 °C could not fully be reached. A verification of the calculations was done in a mock-up test using pure Li_2TiO_3. Subsequently, the irradiation rig design was slightly adapted for the LT- and the HT-irradiations resulting in calculated target temperatures of 397±19 °C and 899±41 °C. The start of the irradiation is planned for spring 2025.

CRediT authorship contribution statement

A. Shaimerdenov: Conceptualization, Supervision, Writing – original draft. **J. Leys:** Conceptualization, Project administration, Validation, Visualization, Writing – original draft. **T. Kulsartov:** Writing – review & editing, Methodology, Conceptualization. **D. Sairanbayev:** Methodology, Investigation. **Y. Chikhray:** Methodology, Investigation. **A. Akhanov:** Visualization, Investigation, Formal analysis. **S. Askerbekov:** Visualization, Investigation, Formal analysis. **M. Ionescu-Bujor:** Writing – review & editing, Project administration, Funding acquisition. **R. Knitter:** Conceptualization, Funding acquisition, Project administration, Resources, Supervision, Writing – review & editing.

Declaration of competing interest

The authors declare that they have no known competing financial interests or personal relationships that could have appeared to influence the work reported in this paper.

Acknowledgements

The authors thank Jin-Hun Park and Dieter Leichtle from KIT-INR for providing essential neutronic calculations to determine the foundation of desired parameters. This work has been carried out within the framework of the EUROfusion Consortium, funded by the European Union via the Euratom Research and Training Programme (Grant Agreement No 101052200 — EUROfusion). Views and opinions expressed are however those of the author(s) only and do not necessarily reflect those of the European Union or the European Commission. Neither the European Union nor the European Commission can be held responsible for them.

Data availability

The authors are unable or have chosen not to specify which data has been used.

References

[1] R. Knitter, M.H.H. Kolb, U. Kaufmann, A.A. Goraieb, Fabrication of modified lithium orthosilicate pebbles by addition of titania, J. Nucl. Mater. 442 (2013) 433–436, https://doi.org/10.1016/j.jnucmat.2012.10.034.

[2] O. Leys, J.M. Leys, R. Knitter, Current status and future perspectives of EU ceramic breeder development, Fusion Eng. Des. 164 (2021) 112171, https://doi.org/10.1016/j.fusengdes.2020.112171.

[3] K. Mukai, P. Pereslavtsev, U. Fischer, R. Knitter, Activation calculations for multiple recycling of breeder ceramics by melt processing, Fusion Eng. Des. 100 (2015) 565–570, https://doi.org/10.1016/j.fusengdes.2015.08.007.

[4] O. Leys, T. Bergfeldt, M.H.H. Kolb, R. Knitter, A.A. Goraieb, The reprocessing of advanced mixed lithium orthosilicate/metatitanate tritium breeder pebbles, Fusion Eng. Des. 107 (2016) 70–74, https://doi.org/10.1016/j.fusengdes.2016.04.025.

[5] A. Zarins, O. Valtenbergs, G. Kizane, A. Supe, R. Knitter, M.H.H. Kolb, O. Leys, L. Baumane, D. Conka, Formation and accumulation of radiation-induced defects and radiolysis products in modified lithium orthosilicate pebbles with additions of titanium dioxide, J. Nucl. Mater. 470 (2016) 187–196, https://doi.org/10.1016/j.jnucmat.2015.12.027.

[6] S. Pupeschi, R. Knitter, M. Kamlah, Effective thermal conductivity of advanced ceramic breeder pebble beds, Fusion Eng. Des. 116 (2017) 73–80, https://doi.org/10.1016/j.fusengdes.2017.01.026.

[7] J.M. Heuser, M.H.H. Kolb, T. Bergfeldt, R. Knitter, Long-term thermal stability of two-phased lithium orthosilicate/metatitanate ceramics, J. Nucl. Mater. 507 (2018) 396–402, https://doi.org/10.1016/j.jnucmat.2018.05.010.

[8] I. Kenzhina, T. Kulsartov, R. Knitter, Y. Chikhray, Y. Kenzhin, Z. Zaurbekova, A. Shaimerdenov, G. Kizane, A. Zarins, A. Kozlovskiy, M. Gabdullin, A. Tolenova, E. Nesterov, Analysis of the reactor experiments results on the study of gas evolution from two-phase Li_2TiO_3-Li_4SiO_4 lithium ceramics, Nucl. Mater. Energy 30 (2022) 101132, https://doi.org/10.1016/j.nme.2022.101132.

[9] T. Kulsartov, Z. Zaurbekova, R. Knitter, Y. Chikhray, I. Kenzhina, S. Askerbekov, A. Shaimerdenov, G. Kizane, Reactor experiments on irradiation of two-phase lithium ceramics Li_2TiO_3/Li_4SiO_4 of various ratios, Fusion Eng. Des. 197 (2023) 114035, https://doi.org/10.1016/j.fusengdes.2023.114035.

[10] Y. Chikhray, S. Askerbekov, R. Knitter, T. Kulsartov, A. Shaimerdenov, M. Aitkulov, A. Akhanov, D. Sairanbayev, Z. Bugybay, A. Nessipbay, K. Kisselyov, G. Kizane, A. Zarins, Studies of irradiated two-phase lithium ceramics Li_4SiO_4/Li_2TiO_3 by thermal desorption spectroscopy, Nucl. Mater. Energy 38 (2024) 101621, https://doi.org/10.1016/j.nme.2024.101621.

[11] T. Kulsartov, I. Kenzhina, R. Knitter, J. Leys, Z. Zaurbekova, A. Shaimerdenov, S. Askerbekov, M. Aitkulov, A. Yelishenkov, A. Yevdakova, T. Zholdybayev, Influence of various gases and water vapors on the processes of tritium release from two-phase lithium ceramics, Fusion Eng. Des. 202 (2024) 114302, https://doi.org/10.1016/j.fusengdes.2024.114302.

[12] T. Kulsartov, Z. Zaurbekova, R. Knitter, I. Kenzhina, Y. Chikhray, A. Shaimerdenov, S. Askerbekov, G. Kizane, A. Yelishenkov, T. Zholdybayev, Comparative analysis of gas release from biphasic lithium ceramics pebble beds of various pebbles sizes and content under neutron irradiation conditions, Nucl. Mater. Energy 38 (2024) 101583, https://doi.org/10.1016/j.nme.2024.101583.

[13] A.A. Shaimerdenov, D.A. Nakipov, F.M. Arinkin, Sh.Kh. Gizatulin, P.V. Chakrov, Ye.A. Kenzhin, The 50th anniversary of the WWR-K research reactor, Phys. Atom. Nucl. 81 (2018) 1408–1411, https://doi.org/10.1134/S1063778818100162.

[14] A. Shaimerdenov, Sh. Gizatulin, D. Dyussambayev, S. Askerbekov, I. Kenzhina, The WWR-K reactor experimental base for studies of the tritium release from materials under irradiation, Fusion Sci. Technol. 76 (2020) 304–313, https://doi.org/10.1080/15361055.2020.1711852.

[15] H. Völlenkle, A. Wittmann, H. Nowotny, Die Kristallstruktur von Li_4SiO_4, Monatshefte der Chemie/Chemical Monthly 99 (1968) 1360–1371, https://doi.org/10.1007/BF00902680.

[16] K. Kataoka, Y. Takahashi, N. Kijima, H. Nagai, J. Akimoto, Y. Idemoto, K. Ohshima, Crystal growth and structure refinement of monoclinic Li_2TiO_3, Mater. Res. Bull. 44 (2009) 168–172, https://doi.org/10.1016/j.materresbull.2008.03.015.

[17] J.H. Park and D. Leichtle, personal communication, October 2022.

[18] C.J. Werner, J.S. Bull, C.J. Solomon, F.B. Brown, G.W. McKinney, M.E. Rising, L. Casswell, MCNP version 6.2 release notes, Los Alamos National Laboratory, 2018, report LA-UR-18-20808, doi:10.2172/1419730.

[19] M.B. Chadwick, M. Herman, P. Obložinský, M.E. Dunn, Y. Danon, A.C. Kahler, P. G. Young, ENDF/B-VII.1 nuclear data for science and technology: cross sections, covariances, fission product yields and decay data, Nuclear data sheets 112 (2011) 2887–2996, https://doi.org/10.1016/j.nds.2011.11.002.

[20] N. Soppera, E. Dupont, M. Fleming, JANIS Book of neutron-induced cross-sections, OECD NEA Data Bank, 2020, Retrieved from https://www.oecd-nea.org/janis/book/book-neutron-2020-09.pdf.

[21] D. Leichtle, Displacement damage parameters for fusion breeder blanket materials based on BCA computer simulations, J. Nucl. Mater. 793 (2002) 307–311, https://doi.org/10.1016/S0022-3115(02)00999-6.

[22] D. Leichtle, Damage parameters and cross sections for Li_4SiO_4/… Li_2TiO_3, Internal reports, in: Forschungszentrum Karlsruhe, now: Karlsruhe Institute of Technology, 1999.

[23] COMSOL Multiphysics® Simulation Software, website last revised 2024, https://www.comsol.com/comsol-multiphysics.

[24] J.T. Van Lew, On thermal characterization of breeder pebble beds with microscale numerical modeling of thermofluid and pebble-pebble interactions, University of California, 2016. PhD Thesis, https://escholarship.org/uc/item/332285gp.